Electron Induced Nanoscale Nuclear Spin Relaxation Probed by Hyperpolarization Injection

William Beatrez,[1] Arjun Pillai,[1] Otto Janes,[1] Dieter Suter,[2] and Ashok Ajoy[1,3,4,*]
[1]Department of Chemistry, University of California, Berkeley, Berkeley, California 94720, USA
[2]Fakultät Physik, Technische Universität Dortmund, D-44221 Dortmund, Germany
[3]Lawrence Berkeley National Laboratory, Chemical Sciences Division, Berkeley, California 94720, USA
[4]CIFAR Azrieli Global Scholars Program, 661 University Ave, Toronto, ON M5G 1M1, Canada

(Received 14 July 2022; accepted 7 June 2023; published 7 July 2023)

We report on experiments that quantify the role of a central electronic spin as a relaxation source for nuclear spins in its nanoscale environment. Our strategy exploits hyperpolarization injection from the electron as a means to controllably probe an increasing number of nuclear spins in the bath and subsequently interrogate them with high fidelity. Our experiments are focused on a model system of a nitrogen vacancy center electronic spin surrounded by several hundred ^{13}C nuclear spins. We observe that the ^{13}C transverse spin relaxation times vary significantly with the extent of hyperpolarization injection, allowing the ability to measure the influence of electron-mediated relaxation extending over several nanometers. These results suggest interesting new means to spatially discriminate nuclear spins in a nanoscale environment and have direct relevance to dynamic nuclear polarization and quantum sensors and memories constructed from hyperpolarized nuclei.

DOI: 10.1103/PhysRevLett.131.010802

Introduction.—Coupled electron-nuclear spin systems are highly relevant in quantum information science [1–3] and dynamic nuclear polarization (DNP) [4]. Consider an electronic spin centrally located (position $r = 0$) in a bath of nuclear spins within a magnetic field B_0 [see Figs. 1(a) and 1(b)]. The electrons are fast relaxing (short T_{1e}) and can serve as a relaxation source for the nuclear spins [5–7] [schematically shown in Fig. 1(c)]. Such electron induced nuclear relaxation is an important consideration for applications in quantum registers, memories, and sensors constructed out of nuclear spins [8–10]. It also plays a key role in determining rates of polarization transfer in DNP [11–13]. However, probing such relaxation influences, particularly in a spatially defined manner, is challenging. This is because experiments typically have very restricted access to spins in the bath, limiting the possibility of spatially distinguishing them [7,14–17]. Previous nanoscale quantum sensing experiments have, for instance, been limited to proximal central spin relaxation effects in small (< 20) spin networks [18,19].

In this Letter, we report on experiments that study the effects of an electronic spin on nuclei over wider length scales, spanning several nanometers, and involving several hundred nuclei. Our strategy [Fig. 1(d)] exploits controllable hyperpolarized spin injection from the electron to the nuclear bath. The hyperpolarization time τ is employed as a knob to tune length scales in the bath being probed; the polarization is carried over longer distances with increasing τ. Simultaneously, the nuclei are subject to a rf driving protocol that permits continuously tracking their magnetization over minute long periods with high signal-to-noise ratio (SNR) [23]. The measurements reveal, surprisingly, that ensemble-averaged nuclear lifetimes T_2' in the rotating frame increase dramatically with increasing polarization time τ. This constitutes a direct experimental signature of electron induced nuclear spin relaxation, allowing us to quantify its influence over several nanometers.

System and protocol.—Experiments are carried out in diamond, with central nitrogen vacancy (NV) [24,25] electronic spins surrounded by ^{13}C nuclei [Figs. 1(a) and 1(b)]. NV centers ($\approx$1 ppm) are separated by $\approx$12 nm and ^{13}C nuclei appear with lattice density $\approx$0.92 spins/nm^3, yielding a relative NV:^{13}C ratio $\sim 1:10^4$ [26,27]. In addition, the lattice hosts randomly positioned paramagnetic impurities (P1 centers) at a concentration > 20 ppm, which can also serve as relaxation sources.

Experiments are conducted in three regimes [indicated in Fig. 1(d)]: (I) optically induced NV $\rightarrow$ ^{13}C spin injection for period τ at low field ($B_{\rm pol} = 36$ mT), (II) rapid transport to high field, and (III) ^{13}C interrogation for time t at $B_0 = 7$ T. For hyperpolarization [Fig. 1(e)], we exploit a mechanism previously described in Refs. [20,21,28]. Distant spins are polarized by spin diffusion driven by the internuclear dipolar Hamiltonian [17,29,30], $\mathcal{H}_{\rm dd} = \sum_{j<k} d_{jk}^{\rm CC}(3I_{jz}I_{kz} - \vec{I}_j \cdot \vec{I}_k)$, where I_j refer to jth spin-1/2 operators and ^{13}C-^{13}C (CC) coupling strengths $d_{jk}^{\rm CC} \propto \gamma_n^2/r^3$, with magnetogyric ratio $\gamma_n = 10.7$ MHz/T, and r being the internuclear distance. Bulk averaged ^{13}C hyperpolarization under maximal conditions is $\varepsilon \approx 0.3\%$.

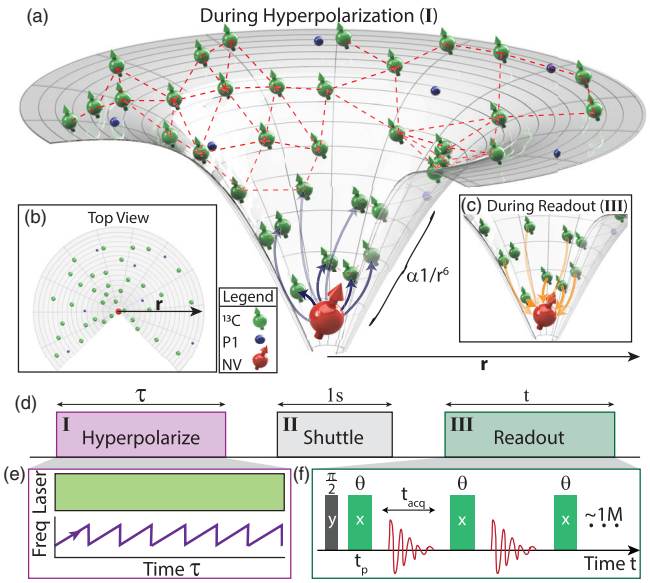

FIG. 1. System and protocol. (a)–(c) System consists of central NV electron (red) and ^{13}C nuclei (green) and P1 centers (blue) at distance r. Dashed lines are internuclear dipolar couplings. Profile denotes $1/r^6$ NV-mediated relaxation effect. (a),(c) NV acts as polarization source and relaxation sink, respectively, during different experimental regimes. (d) Experiment schematic: (I) NV $\rightarrow$ ^{13}C hyperpolarization for period τ at 36 mT, (II) transport to high field, and (III) ^{13}C readout for time t at 7 T. (e) Hyperpolarization (I) involves microwave chirps [20,21]. (f) Measurement (III) comprises a train of spin-locking ϑ pulses with interrogation in t_{acq} interpulse intervals [22]. Note: Time τ describes hyperpolarization time and time t describes readout time.

Sample transport (regime II) occurs in $t_s \approx 1\ \mathrm{s} \ll T_{1n}$, adiabatic with respect to the instantaneous ^{13}C Larmor frequency, thereby preserving hyperpolarization [31]. Conversely, since $t_s \gg T_{1e} \sim 1$ ms [32,33], the NV center rapidly loses hyperpolarization and ultimately returns to thermal levels ($\approx$3%) in regime III [Fig. 1(f)]. Subsequently, the NV center predominantly serves as a point relaxation source for the nuclear bath [Fig. 1(c)].

Ensemble ^{13}C readout (regime III) employs a protocol described in Refs. [22,34]. ^{13}C spins are prepared along the transverse axis $\hat{\mathbf{x}}$ ($\rho_I = \varepsilon \sum_j I_{jx}$) on the Bloch sphere, and a train of spin-locking ϑ pulses are applied [35,36]. ^{13}C nuclei are interrogated between pulses, allowing continuous tracking with high SNR (see Supplemental Material [37]). Signal obtained corresponds to measuring the survival probability in the $\hat{\mathbf{x}}$-$\hat{\mathbf{y}}$ plane. The sequence operation can be described by the unitary $U(t)$. For sufficiently rapid pulsing duty cycle, $U(t) \approx \exp(i\mathcal{H}_F^{(0)} t)$, such that the internuclear Hamiltonian is engineered to leading order in the Magnus expansion to $\mathcal{H}_F^{(0)} \approx \sum_{j<k} d_{jk}^{\mathrm{CC}} (\frac{3}{2}\mathcal{H}_{\mathrm{ff}} - \vec{I}_j \cdot \vec{I}_k)$, where $\mathcal{H}_{\mathrm{ff}} = I_{jz}I_{kz} + I_{jy}I_{ky}$ is a flip-flop Hamiltonian [22]. Since $[\rho_I, \mathcal{H}_F^{(0)}] = 0$ commutes with the initial state, dipolar evolution is suppressed to leading order. As a result, ^{13}C free induction decay lifetimes $T_2^* \sim 1.5$ ms are significantly extended, here to $T_2' \gtrsim 65.5$ s [see Fig. 2(a)].

Results.—Figure 2(a) describes our primary experimental result (see video [38]), showing ^{13}C NMR signal measured employing differing hyperpolarization periods τ (varied every 1 s from $\tau = 1$ to $\tau = 120$ s). Each 36 s trace consists of ~369 000 pulses (see Fig. 3 for full data), and the ^{13}C nuclei are interrogated after every pulse [Fig. 1(f)]. Surprisingly, we observe that the signals decay *more slowly* with increasing τ. Normalization of the signal profiles allows the ability to unravel the *relative* changes in the decay time constant T_2', estimated from the $1/e$ intercept [horizontal dashed line in Fig. 2(a)]. For example, comparing $\tau = 2$ and $\tau = 120$ s in Fig. 2(a), we observe a $\approx$6.42-fold increase in T_2' (from 10.2 to 65.5 s).

The $1/e$ intercept is blind to the instantaneous change of the decay profile and therefore provides only limited information. To more clearly observe the decay dynamics, we divide the curves in Fig. 2(a) into 36 segments of width $\Delta t = 1$ s, with one such segment shown in the gray window in Fig. 2(a). We fit the decay in each segment to a monoexponential [as in inset (i)] and extract the *instantaneous* time constants $T_2(t)$, which are plotted in Fig. 2(b). The notation T_2 (as opposed to T_2') emphasizes that these are monoexponential constants. For each trace, the signals decay markedly slower with increasing time t (see also Fig. 3). Ultimately, the T_2 times are remarkably long ($T_2 \approx 100$ s) at large τ. Increasing polarization time τ makes the overall decay slower for any selected segment. Indeed, for the segment ending at $t = 16$ s [vertical dashed line in Fig. 2(b)], the T_2 value is increased by 1.66-fold. To now emphasize the relative change in the T_2 values for different segments, Fig. 2(c) shows the T_2 lifetimes plotted against τ, where data corresponding to each segment in

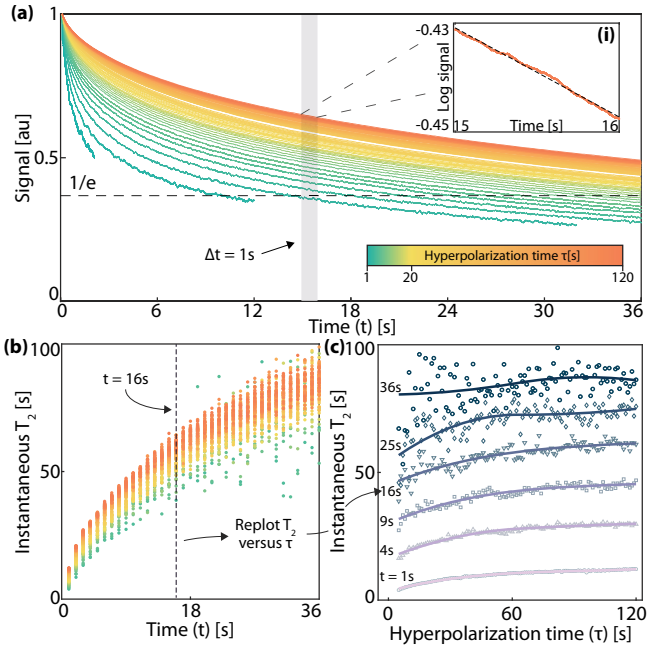

FIG. 2. Effect of increasing hyperpolarization time τ. (a) Spin-lock decays for different hyperpolarization times τ corresponding to color bar [regime I in Fig. 1(d)]. Single-shot data [obtained with $t_{\mathrm{acq}} = 32$ μs and $\vartheta \approx \pi/2$ in Fig. 1(f)] is boxcar averaged over 97 ms and normalized after truncation at $t = 9.7$ ms. Dashed line represents $1/e$ intercept. Inset (i): Enlarged representative 1 s segment [gray window in (a)]. Dashed line is a fitted piecewise monoexponential. (b) Instantaneous lifetime T_2 measured along decay curve, extracted from slopes as in the inset of (a). Color bar [see (a)] represents τ. Dashed line shows exemplary segment ending at 16 s [gray window in (a)]. (c) Instantaneous T_2 plotted against τ. Points show T_2 lifetimes from (b) for exemplary 1 s segments ending at labeled t values. Lines are spline fits.

Figs. 2(a) and 2(b) form the lines. Figure 2(c) makes clear that the instantaneous T_2 increases for each segment with increasing t and within each segment with increasing τ. The maximum relative change occurs for short τ and at early t.

A clearer view of data in Fig. 2 can be obtained by noting that the decays approximately follow a stretched exponential of the form $\exp[-(t/T_2')^{\alpha}]$ with $\alpha \approx 1/2$ (see Fig. 3 and videos [39,40]). While similar behavior has been alluded to before [41–43], high SNR and rapid data collection here allows an unprecedentedly clear view. Figure 3(a) shows data from Fig. 2 plotted on a logarithmic scale with respect to $\sqrt{t}$. The signals then manifest as approximately straight lines, demonstrating stretched exponential character. T_2' lifetimes can now be extracted conveniently from the instantaneous slopes s, as $T_2' = 1/s^2$. High SNR and rapid data collection rates allow the unique ability to continuously observe the stretched exponential dynamics. We now focus attention on six segments along the decay curves [labeled (i)–(vi) in Fig. 3(a)]. Data reveal that the decay in segment (i) deviates from the stretched exponential behavior (especially for low hyperpolarization time τ), as evidenced by the nonlinear traces in the log vs $\sqrt{t}$ representation. In contrast, the traces at long time t are observed to be independent of τ [evident from the approximately parallel profiles in segment (vi)]. To elucidate this further, segment (i) is enlarged in Fig. 3(b) on the same log scale for representative values of τ. The panel makes clear the apparent change in T_2' with τ (due to deviation from stretched exponential decay at short t and τ).

Figure 3(c) shows extracted T_2' values for six segments (i)–(vi). $T_2'^{(i)}$ apparently grows significantly with increasing time τ, while $T_2'^{(vi)}$ is flat and almost independent of τ. Additionally, the extracted T_2' values for the different segments cross over at $\tau \approx 32$ s. Finally, Fig. 3(d) offers insight into variation from exact $\alpha = 1/2$ stretched exponential behavior with changing τ. At long times t, the behavior follows a *universal* $\alpha = 1/2$ dependence (dashed lines). However, in the short time region ($t \lesssim 36$ s), there is a transition from convex to concave behavior around $\alpha = 1/2$. Crossover occurs at $\tau \approx 32$ s, similar to Fig. 3(c).

Theory.—To describe the experimental observations, we construct a semiquantitative model for nuclear polarization $p(r,t)$ at coordinate r and time t. We assume centrosymmetry, a good approximation given the ensemble average in our experiments. We then model the dynamics using the differential equation,

$$\frac{\partial}{\partial t}p(r,t) = \frac{P_0}{r^6} - \frac{\kappa_0}{r^6}p(r,t) - \frac{1}{T_1}p(r,t) + D\nabla^2 p(r,t), \quad (1)$$

following the Bloembergen model in nonconducting solids [44]. Here P_0 denotes the rate of hyperpolarization injection and κ_0 is the strength of spatially dependent relaxation due to the central NV center. The $1/r^6$ scaling of the P_0 term in Eq. (1) does not yield qualitatively different behavior compared to a $1/r^3$ scaling but makes the equation better conditioned near $r = 0$. In any case, the $r \to 0$ region and associated frozen core is not observable due to the relatively small ^{13}C detection bandwidth (≈32 kHz) employed. In contrast to the NV center (at $r = 0$), we assume that the relatively dense P1 centers serve as contributors to *background* relaxation of the ^{13}C nuclei independent of their position; this is captured by the T_1 term in Eq. (1). Finally, the last term denotes spin diffusion, which we assume to be Fickian and Gaussian with a single constant D at all locations. This is a good approximation given the large number of ^{13}C nuclei around every NV center [17]; e.g., a sphere of radius 4 nm contains ≈247 nuclear spins.

We solve Eq. (1) separately in the three regimes of the experiment [Fig. 1(d)], with the solution for one regime setting the initial conditions for the next. Obtaining a precise estimate of the parameters in Eq. (1) is challenging and outside the scope of this Letter. We therefore make some simplifying assumptions. In regime I, we assume

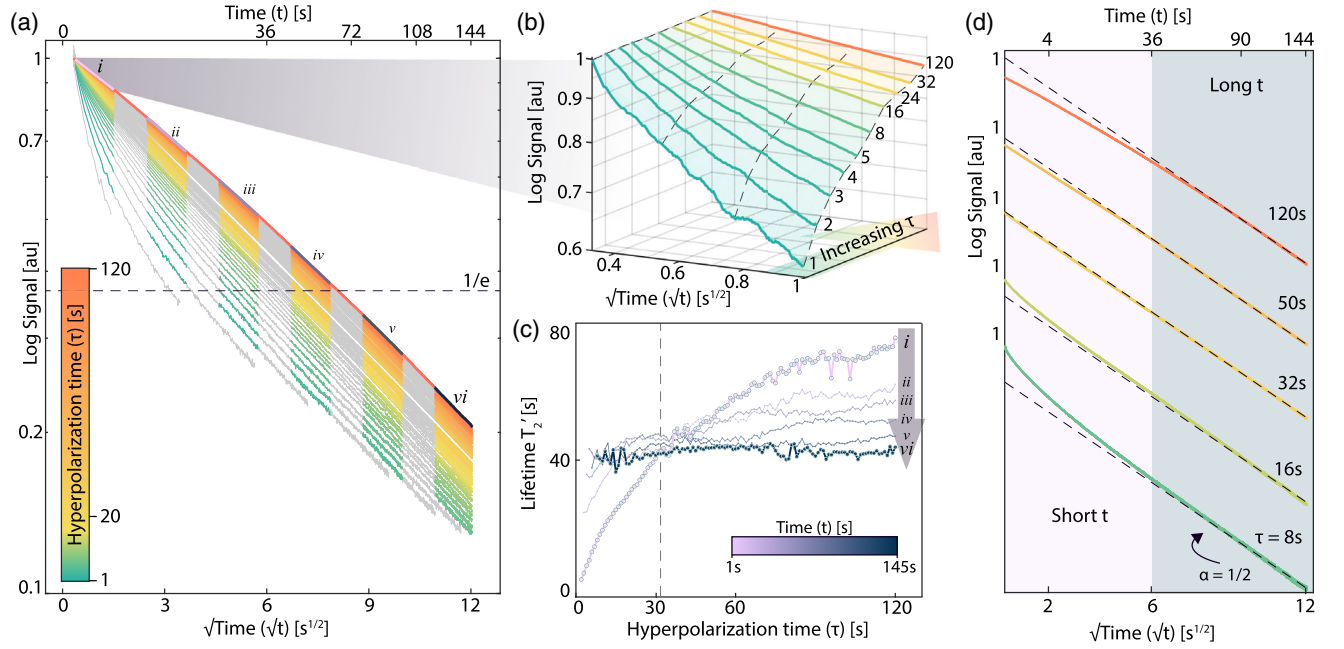

FIG. 3. Quantifying instantaneous decay rates. (a) Full data in Fig. 2 plotted on a log scale with respect to $\sqrt{t}$ for different τ (color bar). Traces extending to $t = 144$ s have $\sim 10^6$ points. Upper axis shows time t. Six equally sized (in $\sqrt{t}$) segments [labeled (i)–(vi)] are selected. (b) Enlargement of segment (i) (sampled every $\approx$5 ms) for representative marked τ values [same color bar as (a)]. Dashed lines are at equally spaced $\sqrt{t}$ values to guide the eye. (c) Extracted time constants T_2' from slopes of the corresponding segments in (a). Segment (i) shows a steep increase in T_2' with τ; subsequent segments show progressively flatter profiles (gray arrow). Crossover of early and late segments occurs at $\tau \approx 32$ s (dashed line). (d) Variations in short and long time decay behavior with τ. At long t, decay closely follows $\alpha = 1/2$ [dashed lines, extracted from segment (vi)], while short times t show a transition from convex to concave behavior at $\tau \approx 32$ s [similar to Fig. 3(c)]. Upper axis represents time t.

$P_0/\kappa_0 = 1$. D in regimes I and III are assumed to differ by a factor of 2. We employ $T_1 = q^{-1}T_{1,\mathrm{LF}}$ and $T_1 = q^{-1}T_{1,\mathrm{HF}}$ in regime I and III, respectively, where $T_{1,\mathrm{LF}} = 283$ s and $T_{1,\mathrm{HF}} = 1520$ s are measured low and high field bulk ^{13}C lifetimes at $\tau = 60$ s (see Supplemental Material [37]), and q is a scaling factor employed as a free parameter in the fits. For Fig. 4, we find good agreement with $q = 6.75$. The latter assumption can be rationalized by the fact that (1) contributions from P1 centers to T_1 relaxation are hard to separate in the bulk T_1 measurements; (2) we measure longitudinal $T_{1,\mathrm{HF}}$, which only approximates transverse T_1 in Eq. (1); and (3) $T_{1,\mathrm{LF}}$ is measured under dark conditions, but the corresponding T_1 in regime I is measured under optical illumination.

With these assumptions, Figs. 4(a) and 4(b) show the simulated system dynamics, where we plot the polarization contained in a shell at radius r, $\mathcal{P} = 4\pi r^2 p$. Figure 4(a) first shows $\mathcal{P}(r,\tau)$ with increasing hyperpolarization time τ in regime I, assuming a 1 s shuttling period in regime II. Simulation parameters are set to obtain good qualitative agreement with experiment (here $D = 0.0135$ nm^2/s and $P_0 = 6.75$ s^{-1}). With increasing τ, spin diffusion leads to a spread of polarization; this is evidenced by the movement of the "centroid" of $\mathcal{P}(r,\tau)$ with increasing τ toward greater r in Fig. 4(a). Notably, however, replenishment of polarization from the NV in regime I makes $\mathcal{P}(r,\tau)$ skew toward the left. In a complementary manner, Fig. 4(b) elucidates $\mathcal{P}(r,t)$ during regime III, starting with the $\tau = 120$ s distribution in Fig. 4(a). The strong relaxing effect of the NV center yields the polarization "hole" close to $r = 0$ and manifests as the steep wall of growing polarization in Fig. 4(b). Additionally, the centroid of $\mathcal{P}(r,t)$ moves toward larger r and homogenizes as t increases; the shift with r is greater here because there is no polarization replenishment and relaxation is slower for larger r.

Figure 4(c) displays the net polarization $\int \mathcal{P}(r,t)dr$ during the readout period [from trajectories as in Fig. 4(b)], but for varying τ. Normalizing the traces shows that relaxation is slower with increasing τ, matching experiments in Fig. 2(a). This arises because the shifting centroid of $\mathcal{P}$ makes electron-mediated relaxation less effective. Interestingly, we find that the decays in Fig. 4(c) also follow an $\alpha = 1/2$ stretched exponential. This is shown by again plotting the data on a log vs $\sqrt{t}$ scale in Fig. 4(d), where we observe a behavior similar to experiments in Fig. 3(a). We hypothesize that the stretched exponential decay at long times t results from the relatively flat distribution of polarization across shells. However, we again see a deviation from stretched exponential decay at short times t and τ (also observed experimentally).

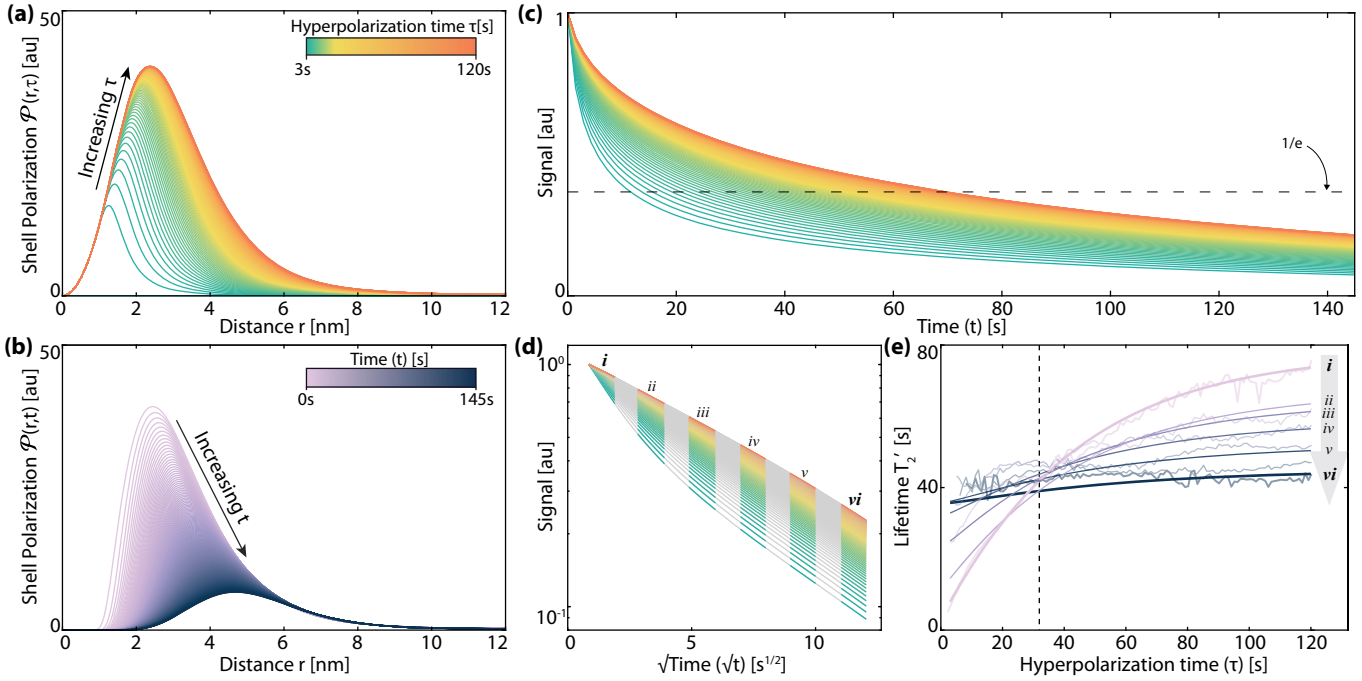

FIG. 4. Simulations of polarization evolution in time and space. (a) Spatial polarization buildup with τ (color bar) plotting polarization $\mathcal{P}(r,\tau)$ in a shell at distance r from the central NV center [during regime I in Fig. 1(d)]. (b) Polarization distribution during readout period t (color bar) in regime III of Fig. 1(d). Here, we set the initial condition to be the $\tau = 120$ s polarization distribution in (a). (c) Simulated NMR signals following (a) and (b) for different hyperpolarization times τ similar to Fig. 2(a). Data reveal T_2' increase with τ, in agreement with the experimental data in Fig. 2 [see (a) for color bar]. (d) Stretched exponential decay dynamics. Analogous to Fig. 3(a), data from (c) are plotted on a logarithmic scale with respect to $\sqrt{t}$. Stretched exponential behavior qualitatively matches data in Fig. 3(a). Segments labeled (i)–(vi) are used to extract T_2' decay constants. (e) Extracted T_2' decay constants for representative segments (i)–(vi) show qualitative agreement with Fig. 3(c). Here, dark lines are simulation and light lines are experimental data. Dashed line marks crossover at $\tau \sim 32$ s.

We attribute this early time behavior to relaxation from NV centers: the deviation is larger at low t and τ when the polarization is localized near the NV centers than at long t and τ when the centroid of $\mathcal{P}$ is further from the NVs [verified by distributions in Figs. 4(a) and 4(b)]. The emergence of a stretched exponential distribution from a large sum of individually monoexponential decays is verified numerically.

As shown in experiments in Fig. 3, the relaxation profile is independent of τ at long readout periods t [evidenced by the approximately parallel traces in segment (vi) of Fig. 4(d)]. Figure 4(b) allows us to verify that this is indeed because the polarization has spread far from the NV center and the decay is instead predominantly due to background $1/T_1$ relaxation. Indeed, as shown in Fig. 4(e), upon taking segments (i)–(vi) along the decay curves in Fig. 4(d) and extracting their T_2' values, we observe a progressive flattening of the T_2' values with increasing τ, agreeing with experimental data in Fig. 3(c) (overlapped here).

Outlook.—Figure 4 suggests that spin-lock control enables the ability to peer into nuclear polarization localized at different positions r with respect to the central electron. Moving through time t in the decay curve corresponds to shifting the sensitive region in the lattice being probed. This suggests a (nonlinear) means to map from t to an effective r coordinate, suggesting a method of discriminating nuclei in the electronic environment. Furthermore, Fig. 3 indicates that nuclear spins can probe electronic relaxation processes, potentially offering a view into the phonon density of states that dominate these relaxation mechanisms [33,45–47]. This is relevant to molecular systems [48–51] and in DNP, wherein the concentration and identity of electron spins can vastly affect nuclear polarization levels [52,53].

A. A. acknowledges funding from ONR (N00014-20-1-2806), AFOSR (22RT0619) and CIFAR Azrieli Global Scholars Fellowship (GS23-013). W. B. acknowledges support from the NSF Graduate Research Fellowship.

*ashokaj@berkeley.edu

[1] N. V. Prokof'ev and P. C. E. Stamp, Theory of the spin bath, Rep. Prog. Phys. **63**, 669 (2000).

[2] T. Ladd, F. Jelezko, R. Laflamme, Y. Nakamura, C. Monroe, and J. L. O'Brien, Quantum computers, Nature (London) **464**, 45 (2010).

[3] C. L. Degen, F. Reinhard, and P. Cappellaro, Quantum sensing, Rev. Mod. Phys. **89**, 035002 (2017).
[4] A. Abragam and M. Goldman, Principles of dynamic nuclear polarization, Rep. Prog. Phys. **41**, 395 (1978).
[5] W. M. Witzel and S. Das Sarma, Quantum theory for electron spin decoherence induced by nuclear spin dynamics in semiconductor quantum computer architectures: Spectral diffusion of localized electron spins in the nuclear solid-state environment, Phys. Rev. B **74**, 035322 (2006).
[6] N. Bloembergen, E. Purcell, and R. Pound, Nuclear magnetic relaxation, Nature (London) **160**, 475 (1947).
[7] W. Blumberg, Nuclear spin-lattice relaxation caused by paramagnetic impurities, Phys. Rev. **119**, 79 (1960).
[8] R. Hanson, V. V. Dobrovitski, A. E. Feiguin, O. Gywat, and D. D. Awschalom, Coherent dynamics of a single spin interacting with an adjustable spin bath, Science **320**, 352 (2008).
[9] A. Reiserer, N. Kalb, M. S. Blok, K. J. M. van Bemmelen, T. H. Taminiau, R. Hanson, D. J. Twitchen, and M. Markham, Robust Quantum-Network Memory Using Decoherence-Protected Subspaces of Nuclear Spins, Phys. Rev. X **6**, 021040 (2016).
[10] J. J. L. Morton, A. M. Tyryshkin, R. M. Brown, S. Shankar, B. W. Lovett, A. Ardavan, T. Schenkel, E. E. Haller, J. W. Ager, and S. A. Lyon, Solid-state quantum memory using the 31p nuclear spin, Nature (London) **455**, 1085 (2008).
[11] T. A. Siaw, M. Fehr, A. Lund, A. Latimer, S. A. Walker, D. T. Edwards, and S.-I. Han, Effect of electron spin dynamics on solid-state dynamic nuclear polarization performance, Phys. Chem. Chem. Phys. **16**, 18694 (2014).
[12] E. P. Saliba, E. L. Sesti, F. J. Scott, B. J. Albert, E. J. Choi, N. Alaniva, C. Gao, and A. B. Barnes, Electron decoupling with dynamic nuclear polarization in rotating solids, J. Am. Chem. Soc. **139**, 6310 (2017).
[13] A. Sarkar, B. Blankenship, E. Druga, A. Pillai, R. Nirodi, S. Singh, A. Oddo, P. Reshetikhin, and A. Ajoy, Rapidly Enhanced Spin Polarization Injection in an Optically Pumped Spin Ratchet, Phys. Rev. Appl. **18**, 034079 (2022).
[14] D. Tse and S. Hartmann, Nuclear Spin-Lattice Relaxation via Paramagnetic Centers without Spin Diffusion, Phys. Rev. Lett. **21**, 511 (1968).
[15] E. P. Horvitz, Nuclear spin diffusion induced by paramagnetic impurities in nonconducting solids, Phys. Rev. B **3**, 2868 (1971).
[16] Q. Stern, S. F. Cousin, F. Mentink-Vigier, A. C. Pinon, S. J. Elliott, O. Cala, and S. Jannin, Direct observation of hyperpolarization breaking through the spin diffusion barrier, Sci. Adv. **7**, eabf5735 (2021).
[17] C. Ramanathan, Dynamic nuclear polarization and spin diffusion in nonconducting solids, Appl. Magn. Reson. **34**, 409 (2008).
[18] A. Dréau, P. Jamonneau, O. Gazzano, S. Kosen, J.-F. Roch, J. R. Maze, and V. Jacques, Probing the Dynamics of a Nuclear Spin Bath in Diamond through Time-Resolved Central Spin Magnetometry, Phys. Rev. Lett. **113**, 137601 (2014).
[19] M. Abobeih, J. Randall, C. Bradley, H. Bartling, M. Bakker, M. Degen, M. Markham, D. Twitchen, and T. Taminiau, Atomic-scale imaging of a 27-nuclear-spin cluster using a quantum sensor, Nature (London) **576**, 411 (2019).
[20] A. Ajoy, K. Liu, R. Nazaryan, X. Lv, P. R. Zangara, B. Safvati, G. Wang, D. Arnold, G. Li, A. Lin *et al.*, Orientation-independent room temperature optical ^{13}C hyperpolarization in powdered diamond, Sci. Adv. **4**, eaar5492 (2018).
[21] A. Ajoy, R. Nazaryan, K. Liu, X. Lv, B. Safvati, G. Wang, E. Druga, J. Reimer, D. Suter, C. Ramanathan *et al.*, Enhanced dynamic nuclear polarization via swept microwave frequency combs, Proc. Natl. Acad. Sci. U.S.A. **115**, 10576 (2018).
[22] W. Beatrez, O. Janes, A. Akkiraju, A. Pillai, A. Oddo, P. Reshetikhin, E. Druga, M. McAllister, M. Elo, B. Gilbert, D. Suter, and A. Ajoy, Floquet Prethermalization with Lifetime Exceeding 90 s in a Bulk Hyperpolarized Solid, Phys. Rev. Lett. **127**, 170603 (2021).
[23] O. Sahin, H. A. Asadi, P. Schindler, A. Pillai, E. Sanchez, M. Elo, M. McAllister, E. Druga, C. Fleckenstein, M. Bukov *et al.*, Continuously tracked, stable, large excursion trajectories of dipolar coupled nuclear spins, arXiv:2206.14945.
[24] F. Jelezko and J. Wrachtrup, Single defect centres in diamond: A review, Phys. Status Solidi (a) **203**, 3207 (2006).
[25] N. B. Manson, J. P. Harrison, and M. J. Sellars, Nitrogen-vacancy center in diamond: Model of the electronic structure and associated dynamics, Phys. Rev. B **74**, 104303 (2006).
[26] A. Ajoy, B. Safvati, R. Nazaryan, J. Oon, B. Han, P. Raghavan, R. Nirodi, A. Aguilar, K. Liu, X. Cai *et al.*, Hyperpolarized relaxometry based nuclear T_1 noise spectroscopy in diamond, Nat. Commun. **10**, 5160 (2019).
[27] J. Van Wyk, E. Reynhardt, G. High, and I. Kiflawi, The dependences of ESR line widths and spin-spin relaxation times of single nitrogen defects on the concentration of nitrogen defects in diamond, J. Phys. D **30**, 1790 (1997).
[28] A. Ajoy, R. Nazaryan, E. Druga, K. Liu, A. Aguilar, B. Han, M. Gierth, J. T. Oon, B. Safvati, R. Tsang *et al.*, Room temperature "optical nanodiamond hyperpolarizer": Physics, design, and operation, Rev. Sci. Instrum. **91**, 023106 (2020).
[29] A. Karabanov, D. Wiśniewski, I. Lesanovsky, and W. Köckenberger, Dynamic Nuclear Polarization as Kinetically Constrained Diffusion, Phys. Rev. Lett. **115**, 020404 (2015).
[30] Y. Hovav, A. Feintuch, and S. Vega, Theoretical aspects of dynamic nuclear polarization in the solid state–the solid effect, J. Magn. Reson. **207**, 176 (2010).
[31] A. Ajoy, X. Lv, E. Druga, K. Liu, B. Safvati, A. Morabe, M. Fenton, R. Nazaryan, S. Patel, T. F. Sjolander, J. A. Reimer, D. Sakellariou, C. A. Meriles, and A. Pines, Wide dynamic range magnetic field cycler: Harnessing quantum control at low and high fields, Rev. Sci. Instrum. **90**, 013112 (2019).
[32] I. Popa, T. Gaebel, M. Domhan, C. Wittmann, F. Jelezko, and J. Wrachtrup, Energy levels and decoherence properties of single electron and nuclear spins in a defect center in diamond, Phys. Rev. B **70**, 201203(R) (2004).
[33] A. Jarmola, V. M. Acosta, K. Jensen, S. Chemerisov, and D. Budker, Temperature-and Magnetic-Field-Dependent Longitudinal Spin Relaxation in Nitrogen-Vacancy Ensembles in Diamond, Phys. Rev. Lett. **108**, 197601 (2012).
[34] A. Ajoy, R. Nirodi, P. Reshetikhin, E. Druga, A. Akkiraju, M. McAllister, G. Maineri, S. Le, A. Lin, A. M. Souza,

C. A. Meriles, B. Gilbert, D. Suter, J. A. Reimer, and A. Pines, Dynamical decoupling in interacting systems: Applications to signal-enhanced hyperpolarized readout, arXiv:2008.08323.

[35] W.-K. Rhim, D. Burum, and D. Elleman, Multiple-Pulse Spin Locking in Dipolar Solids, Phys. Rev. Lett. **37**, 1764 (1976).

[36] W.-K. Rhim, D. D. Elleman, and R. W. Vaughan, Analysis of multiple pulse NMR in solids, J. Chem. Phys. **59**, 3740 (1973).

[37] See Supplemental Material at http://link.aps.org/supplemental/10.1103/PhysRevLett.131.010802 for further experimental details.

[38] Video showing full dataset of Fig. 2(a): https://www.youtube.com/watch?v=GEdVRV2cXH4 (2021).

[39] Video showing full dataset of Fig. 3(a): https://www.youtube.com/watch?v=b8Be0R2etZQ (2021).

[40] Video showing unnormalized dataset of Fig. 3(a): https://www.youtube.com/watch?v=5tirO0yE4zg (2021).

[41] H. Lock, G. E. Maciel, and C. E. Johnson, Natural-abundance ^{13}C dynamic nuclear polarization experiments on chemical vapor deposited diamond film, J. Mater. Res. **7**, 2791 (1992).

[42] J. S. Hartman, A. Narayanan, and Y. Wang, Spin-lattice relaxation in the 6h polytype of silicon carbide, J. Am. Chem. Soc. **116**, 4019 (1994).

[43] P. M. Henrichs and M. Linder, Carbon-13 spin diffusion in the determination of intermolecular structure in solids, J. Magn. Reson. (1969) **58**, 458 (1984).

[44] N. Bloembergen, On the interaction of nuclear spins in a crystalline lattice, Physica (Amsterdam) **15**, 386 (1949).

[45] S. Takahashi, R. Hanson, J. van Tol, M. S. Sherwin, and D. D. Awschalom, Quenching Spin Decoherence in Diamond through Spin Bath Polarization, Phys. Rev. Lett. **101**, 047601 (2008).

[46] J.-C. Jaskula, K. Saha, A. Ajoy, D. J. Twitchen, M. Markham, and P. Cappellaro, Cross-Sensor Feedback Stabilization of an Emulated Quantum Spin Gyroscope, Phys. Rev. Appl. **11**, 054010 (2019).

[47] M. P. Ledbetter, K. Jensen, R. Fischer, A. Jarmola, and D. Budker, Gyroscopes based on nitrogen-vacancy centers in diamond, Phys. Rev. A **86**, 052116 (2012).

[48] S. Bayliss, D. Laorenza, P. Mintun, B. Kovos, D. Freedman, and D. Awschalom, Optically addressable molecular spins for quantum information processing, Science **370**, 1309 (2020).

[49] A. Henstra and W. T. Wenckebach, Dynamic nuclear polarisation via the integrated solid effect I: Theory, Mol. Phys. **112**, 1761 (2014).

[50] K. Tateishi, M. Negoro, S. Nishida, A. Kagawa, Y. Morita, and M. Kitagawa, Room temperature hyperpolarization of nuclear spins in bulk, Proc. Natl. Acad. Sci. U.S.A. **111**, 7527 (2014).

[51] N. Niketic, B. Brandt, W. T. Wenckebach, J. Kohlbrecher, and P. Hautle, Polarization analysis in neutron small-angle scattering with a novel triplet dynamic nuclear polarization spin filter, J. Appl. Crystallogr. **48**, 1514 (2015).

[52] S. Lange, A. H. Linden, Ü. Akbey, W. T. Franks, N. M. Loening, B.-J. van Rossum, and H. Oschkinat, The effect of biradical concentration on the performance of DNP-MAS-NMR J. Magn. Reson. **216**, 209 (2012).

[53] A. Capozzi, T. Cheng, G. Boero, C. Roussel, and A. Comment, Thermal annihilation of photo-induced radicals following dynamic nuclear polarization to produce transportable frozen hyperpolarized ^{13}C-substrates, Nat. Commun. **8**, 15757 (2017).